doi:10.26443/seismica.v5i2.2860

Frequency-Resolved Seismic Source Localization in Fluvial Settings Using Dense Arrays

Samidha V. Revankar * [1], **Florent Gimbert** [2], **Alain Recking** [1,3]

[1]Université Grenoble Alpes UGA, Institute for Geoscience and Environment (IGE), Grenoble, France, [2]Université Grenoble Alpes, Institute for Geoscience and Environment (IGE), CNRS, Grenoble, France, [3]Université Grenoble Alpes, Institute for Geoscience and Environment (IGE), National Institute for Agriculture and Environment INRAE, Grenoble, France

Author contributions: *Conceptualization*: Samidha Revankar, Florent Gimbert. *Formal Analysis*: Samidha Revankar. *Writing - Original draft*: Samidha Revankar. *Supervision*: Florent Gimbert, Alain Recking.

Abstract Monitoring dynamic surface processes such as sediment transport and turbulence during high-flow events remains a major challenge in fluvial geomorphology. Seismic methods provide a non-invasive alternative, but robust source localization is hindered by the distributed nature of sources, heterogeneous shallow structures, and the broadband character of the emitted signals. Here, we present a generalized framework for frequency-resolved seismic source localization using dense-arrays and matched field processing (MFP). We introduce a hybrid approach that exploits the array differently across frequencies: full-network MFP at low-frequencies, where coherence spans the entire aperture, and sub-array averaging at high-frequencies, where coherence is confined to local scales. Applied to a field case, we observe frequency-dependent source distributions, with spatially widespread sources at low-frequencies consistent with turbulent flow and more localized sources at high-frequencies consistent with bedload impacts, suggesting both source processes can be located simultaneously. We use synthetic tests to quantify localization uncertainty as a function of frequency, sensor density, and signal-to-noise ratio. Across the 2–40 Hz range, uncertainty increases from a few meters at low-frequencies to more than 100 meters at high-frequencies. By quantifying these trade-offs, we provide practical guidance for future deployments, including array geometry and processing required to achieve a target resolution.

Production Editor: Gareth Funning
Handling Editor: Marion Ramos
Copy & Layout Editor: Anna Horleston

Signed reviewer(s): John-Morgan Manos

Received: 24 March 2026
Accepted: 29 September 2026
Published: 20 November 2026

Non-technical summary Rivers generate ground motion as water flows, sediments move, and turbulence develops. These vibrations can be recorded by seismometers placed along riverbanks and provide a way to monitor river processes *in-situ* without disturbing the environment. However, identifying where these signals originate within a river channel is difficult because many competing processes occur at the same time, and the ground structure is complex. In this study, we present a method to locate the sources of river-generated seismic signals using dense arrays of seismometers. By comparing the seismic signals recorded across many sensors in a dense array, we estimate where the vibrations originate within the river channel. By analyzing the signals at different frequencies separately, we locate the sources of different river processes occurring within the channel. Lower-frequency signals are distributed across much of the channel and are consistent with turbulence generated by flowing water. Higher-frequency signals are more localized and are consistent with impacts from moving sediment particles on the riverbed. Through our results, we show that dense seismic arrays can be used for automatic source detection and location of these processes in space, and to provide practical guidance on how sensor arrays should be designed to achieve reliable source localization.

1 Introduction

Dense seismic arrays are gaining popularity across geophysical research for their ability to capture high-resolution spatial and temporal information (Schweitzer et al., 2012; Rost and Thomas, 2002). Several factors have contributed to this rise: improvements in sensor sensitivity and reliability, decreasing costs, and the availability of synchronised multi-channel acquisition systems. Dense arrays are particularly well-suited to recording high-frequency seismic signals (above 1 Hz), where short wavelengths demand dense spatial sampling (Nanni et al., 2022).

To characterize environmental sources, dense seismic arrays have been successfully applied in glacial contexts, where crevassing, basal motion, and subglacial hydrology generate high-frequency seismic signals that propagate through complex, shallow structures (Nanni et al., 2021, 2022, 2024; Gimbert et al., 2021). In fluvial systems, which are arguably just as dynamic and structurally complex, dense arrays have received comparatively less attention. Existing river seismic studies have nonetheless provided important insights into where fluvial seismic energy is predominantly generated at the reach scale. For example, analyses based on seismic amplitude and spectral content have revealed

*Corresponding author: samidha.venkatesh-revankar@univ-grenoble-alpes.fr

along-stream variations associated with active channel segments or enhanced sediment transport (Burtin et al., 2008; Schmandt et al., 2017). Such approaches are particularly effective when integrated over long time windows or broad frequency bands. In addition, correlation-based approaches have been used to infer the dominant locations of river-generated seismic noise by analyzing noise cross-correlation functions between stations (Burtin et al., 2010). However, they are not designed to resolve the spatial and temporal variability of seismic sources at the scale of individual channel features, nor to disentangle multiple coexisting processes acting simultaneously across distinct frequency ranges. This limitation is especially relevant given that rivers generate a wide spectrum of seismic signals, ranging from short impulsive bursts to sustained tremor-like motion, associated with processes such as turbulence, bedload transport, debris flows, and rainfall impacts (Burtin et al., 2008, 2011; Cook et al., 2018; Schmandt et al., 2017; Bakker et al., 2020, 2022). These signals are typically broadband, with energy spanning from a few hertz up to 60 Hz or more (Tsai et al., 2012; Gimbert et al., 2014, 2019).

Understanding river hydro- and morphodynamics requires resolving spatial patterns at the scale of the active channel, typically on the order of tens of meters and comparable to the river width. This is the scale at which flow separation, bar migration, and bedload convergence or divergence occur, and where morphological change is most pronounced during floods (Rodrigues et al., 2015; Ferguson and Ashworth, 1992; Bertoldi et al., 2010). During floods, which are key moments of channel reworking, direct observations are often limited; in-channel instrumentation may be damaged or overwhelmed, while satellite or drone imagery typically provides only snapshots before and after the event (Chmiel et al., 2022; Tao et al., 2024). It is at this intermediate scale, between individual grain impacts and reach-averaged fluxes, that dense seismic arrays have the potential to uniquely capture the dynamics of sediment transport and channel reorganization.

Localizing river-induced seismic sources remains particularly challenging. Seismic energy is expected to arise from multiple, spatially distributed processes acting simultaneously: turbulence, particle impacts, bank collapses, and flow instabilities, all embedded in a heterogeneous, shallow structure (Tsai et al., 2012; Farin et al., 2019; Gimbert et al., 2014). The resulting wavefield is emergent rather than impulsive, dominated by overlapping and temporally variable sources whose coherence changes with frequency. These conditions make it difficult to relate the observed seismic patterns to specific locations or processes, as classical localization approaches rely on stable phase relationships and well-defined point sources. In addition, near-surface scattering and velocity contrasts further distort the wavefield, complicating phase coherence across the array. During flood conditions, such complexities, rather than external noise contamination, are expected to be the primary limitation for source localization.

Common localization approaches include polarization analysis, noise correlation, and array-based stacking methods such as beamforming. Polarization analysis estimates back-azimuths from particle motion (Vidale, 1986; Ali and Bean, 2022; Gonzalez et al., 2023), but becomes unreliable at high frequencies where wavefields are strongly scattered and contain mixed body and surface wave components. Noise correlation techniques (Stehly et al., 2006; Almendros et al., 1999; Burtin et al., 2010) can be used to reconstruct source azimuth from long time series, yet they are most effective at larger scales and may not be suited for resolving short-lived, localized sources within complex near-surface structures. Classical beamforming coherently stacks time-shifted waveforms across the array to enhance weak sources (Cros et al., 2011), but it assumes plane wavefronts, which restricts its validity to far-field conditions. Grid-based methods that model curved, spherical wavefronts are more appropriate for near-field localization and for handling multiple overlapping sources within heterogeneous media (Cros et al., 2011).

One such method is Matched Field Processing (MFP). Originally developed in underwater acoustics (Baggeroer et al., 2002; Tolstoy, 1992; Kuperman and Turek, 1997), MFP has been increasingly applied in near-surface seismology to track weak, non-impulsive, or continuous sources, such as those generated by ice-bed interface processes (Nanni et al., 2024), or hydrothermal fluid flow (Cros et al., 2011). It is a frequency domain operation which compares the observed phase field with a modeled phase field predicted for a known source and an assumed phase velocity, exploiting spatial coherence across the array to estimate a probabilistic distribution of source locations (Chmiel et al., 2019; Nanni et al., 2022). When implemented on dense arrays, MFP offers a robust way to track source evolution over time, even when the signals of interest are complex and prone to scattering.

In this study, we present a methodological framework for frequency-resolved seismic source localization that is applicable to dense arrays in fluvial settings and achieves location precision sufficient to resolve river morphodynamics. We develop a hybrid localization strategy using MFP tailored to the geometry of a dense array deployed along the Séveraisse River, a steep Alpine stream in the French Alps. Source distributions reveal different fluvial processes across distinct frequency bands, allowing turbulence-dominated and bedload-dominated source regions to be resolved within a single deployment, with spatial resolution on the order of tens of meters, sufficient to discriminate between distinct channel-scale processes. We believe this represents a first attempt to perform detailed, frequency-resolved source localization in a fluvial setting during an active geomorphic event. By linking localization performance to factors such as frequency sensitivity, sensor density, and sub-array configuration, we provide guidance that can inform array design in environmental seismology and help target specific processes of interest.

2 Experimental Design

2.1 Field Site

The Séveraisse River is a gravel-bed river located in the Écrins Massif of the French Alps. It flows through an alpine catchment characterized by strong seasonal discharge, driven by snowmelt and episodic rainfall. It has been the object of multiple environmental seismology studies that established quantitative links between seismic ground motion, water flow, and sediment transport. Previous work documented seismic signatures associated with turbulence and low bedload transport at modest discharges (Bakker et al., 2020; Misset et al., 2021), as well as the response of seismic signals to intense bedload transport during extreme flood events (Johannot et al., 2025). For our study, we focus on a 600 m long braided reach of the river, with a maximum active channel width of approximately 90 m (Figure 1). The monitored reach exhibits frequent bar reorganization and active sediment transport, particularly during high-discharge events (Misset et al., 2020a, 2021). This reach is easily accessible and well equipped with a hydrological monitoring station run by Électricité de France (EDF) located approximately 200 m downstream of the study reach, providing discharge measurements at 10-minute resolution. A fixed-position timelapse camera installed on a rocky outcrop downstream of the reach, approximately 64 m above the valley floor, provides continuous visual coverage of the active channel (Figure 4a,b). Rainfall data was also provided by EDF with a temporal resolution of 6 min.

Between July 2 and July 4, 2019, a flood event occurred following a period of sustained snowmelt combined with rainfall, reaching peak discharges of approximately 40 $\mathrm{m^3\,s^{-1}}$, which mobilized significant bed material corresponding to an estimated five-year return period. Such high-energy events are rarely captured in detail, as they often exceed the operational limits of traditional monitoring techniques. In this case, the dense seismic array had been deployed as part of an observational campaign, and the flood occurred during the recording period. In Figure 2a, we summarize the hydrological and seismic context of the July 2019 flood. The top panel presents the 2019 discharge record, highlighting the seismic acquisition period and the flood interval (July 2–5), together with rainfall intensity. The lower panels show the vertical-component seismic record captured by sensor 1 in subarray 1 and its corresponding spectrogram. The seismic data show a broadband increase in power concurrent with rising discharge, with intermittent high-frequency bursts superimposed on a continuous low-frequency background.

2.2 Seismic Array

To monitor seismic energy generated during the flood, a dense seismic array of 3-component Fairfield ZLand nodal seismographs was deployed along the targeted braided section. Sensors were buried entirely with a few centimetres of ground on, to ensure stable coupling and reduce sentivity to rainfall noise (Rindraharisaona et al., 2022). Each sensor recorded continuously at a sampling rate of 250 Hz. They have a low-corner cutoff frequency of 5 Hz and a sensitivity of 76.7 $\mathrm{Vm^{-1}s^{-1}}$, as characterized in laboratory tests (Ringler et al., 2018), with typical power endurance of about 35 days.

The overall design of the dense array was guided by theoretical and practical constraints on spatial sampling and coverage. To avoid spatial aliasing, the interstation distance Δl must be smaller than approximately half the wavelength, expressed as

$$\lambda = \frac{c}{f} \gtrsim 2\Delta l, \tag{1}$$

where λ is the seismic wavelength, c is the phase velocity, and f is the signal frequency. This sets the highest resolvable frequency for a given sensor spacing. Conversely, the lowest resolvable frequency is controlled by the array aperture A, such that wavelengths much larger than the aperture cannot be coherently resolved. For the range of phase velocities relevant to near-surface river sediments ($c \approx$ 200–600 m $\mathrm{s^{-1}}$ (Bakker et al., 2020)) and the frequency band of interest (2–40 Hz), the corresponding wavelengths vary between 5 m and 300 m. To fulfil the condition in equation (1), we design the network with multiple sub-arrays, each consisting of 8 to 9 sensors spaced at approximately Δl = 5 m apart, with subarray aperture, A_{sub} of about 25 m. These sub-arrays were placed to optimize both azimuthal coverage and spatial resolution, while maintaining sensitivity to seismic sources within the active river channel. At the same time, the full network aperture, A_{net}, spans approximately 500 m along the active braided reach, a scale comparable to the morphological units of interest. These configurations were selected to ensure sensitivity to seismic energy in the broad frequency range (Bakker et al., 2020; Piantini et al., 2022), corresponding to dominant frequencies expected from turbulent flow and bedload transport (Nasr et al., 2023, 2024). Figure 2b shows waveforms filtered between 10 and 15 Hz across subarrays 1, 3, 5 and 7. The shaded regions show short, coherent energy packets across these subarrays.

3 Methodology

3.1 Matched Field Processing

Matched Field Processing (MFP) is a frequency-domain seismic source localization technique that exploits differences in arrival times recorded across a seismic array to infer the location of coherent seismic sources (Thode et al., 2000; Nanni et al., 2022; Chmiel et al., 2022; Cros et al., 2011). In practice, the method consists of measuring the relative phase delays between all pairs of sensors for a given short time window, and comparing these observed delays to those predicted for hypothetical sources distributed over a grid of trial locations and associated phase velocities. Source locations and phase velocities are then identified by searching for the configuration for which the predicted delays best match the observed ones. As illustrated in Figure 2b, seismic energy is recorded as short, coherent wave packets that

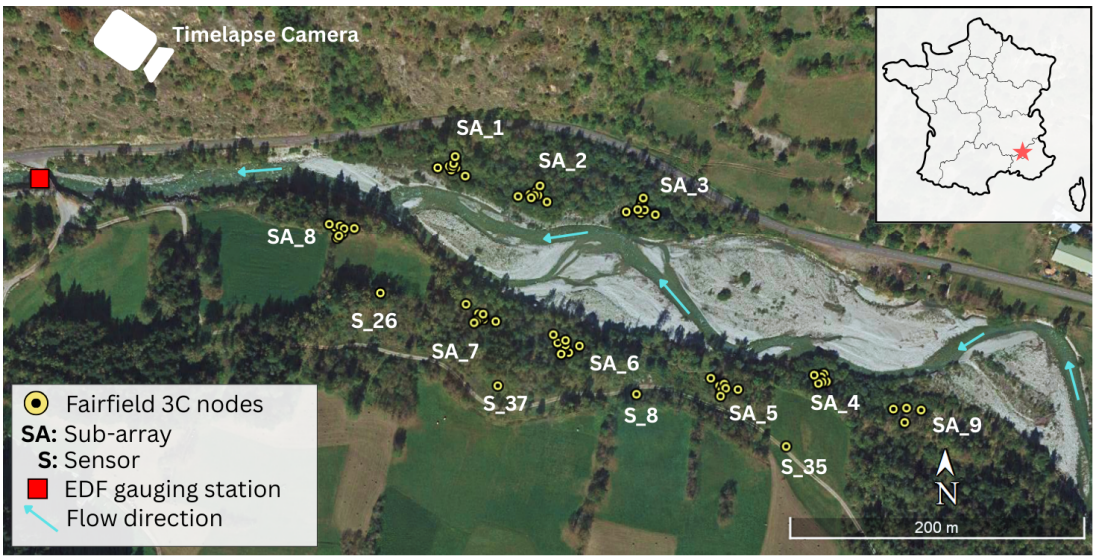


Figure 1 Map of the study area along the Séveraisse River, showing the deployed seismometers, timelapse camera, the EDF gauging station and the extent of the 600 m braided reach monitored during the 2019 flood (Image retrieved from Google Earth)

reach different sensors at slightly different times, forming a consistent wavefront pattern across subarrays. Because this coherence persists only for a few seconds, phase-based localization methods are applied in short time windows.

Given a recorded seismic ground motion time series $d_n(t)$ at N sensors, in frequency domain, we have

$$d_n(\omega) = \mathcal{F}\{d_n(t)\} \tag{2}$$

assembled into a complex data vector

$$\mathbf{d}(\omega) = [d_1(\omega), d_2(\omega), \ldots, d_N(\omega)]^T, \tag{3}$$

which encodes the observed phase relationships across the array at a given frequency. To quantify how coherent the recorded wavefield is between all sensor pairs, we compute the cross-spectral density matrix (CSDM),

$$\mathbf{C}(\omega) = \mathbf{d}(\omega)\,\mathbf{d}^H(\omega), \tag{4}$$

which summarizes the spatial phase coherence of the wavefield across the array. We then locate sources by systematically testing whether the observed phase relationships are consistent with those expected from a hypothetical source at each location of a spatial grid. For a trial source defined by its position $\mathbf{x} = (x, y)$ and a trial phase velocity c, we compute the expected travel times to each sensor and convert them into predicted phase values. These predicted phases are assembled into a synthetic replica vector,

$$\mathbf{g}(\omega, \mathbf{x}, c) = \exp\left(i\omega \frac{\mathbf{r}(\mathbf{x})}{c}\right), \tag{5}$$

where $\mathbf{r}(\mathbf{x})$ contains the source–receiver distances.

The similarity between the observed and predicted phase fields is quantified using the linear Bartlett processor,

$$B(\mathbf{x}, \omega, c) = \frac{1}{N(N-1)} \frac{\left|\mathbf{g}^H(\omega, \mathbf{x}, c)\,\mathbf{C}(\omega)\,\mathbf{g}(\omega, \mathbf{x}, c)\right|}{\left|\mathbf{g}(\omega, \mathbf{x}, c)\right|^2}. \tag{6}$$

Higher values of B indicate stronger phase coherence across the array, and therefore regions where seismic energy contributes coherently at the tested frequency. To improve robustness, we incoherently average the Bartlett processor over a set of frequencies $\omega \in \Omega$,

$$B(\mathbf{x}, c) = \frac{1}{N_\omega\, N(N-1)} \sum_{\omega \in \Omega} \frac{\left|\mathbf{g}^H(\omega, \mathbf{x}, c)\,\mathbf{C}(\omega)\,\mathbf{g}(\omega, \mathbf{x}, c)\right|}{\left|\mathbf{g}(\omega, \mathbf{x}, c)\right|^2}. \tag{7}$$

By construction, B is bounded between 0 and 1 and forms a spatial coherence map (often referred to as an ambiguity surface). Because fluvial seismic sources are spatially distributed rather than strictly point-like, B is interpreted as a relative measure of local phase coherence rather than a probability density.

We apply MFP in non-overlapping 3 s time windows, independently for each 5 Hz-wide frequency band (2–5, 5–10, ..., 35–40 Hz). Accurate localization requires specifying an appropriate phase velocity c for each frequency band and array configuration. Because the shallow velocity structure in the study area is not independently constrained, phase velocities are estimated empirically from the seismic data.

For each band and array configuration (full network or subarray), we repeat the MFP calculation over a range of trial velocities and compute the maximum Bartlett value

$$B_{\max}(c) = \max_{\mathbf{x}}[B(\mathbf{x}; c)]. \tag{8}$$

$$v_{\max}(f) = \operatorname{argmax}_v[B_{\max}(c)] \tag{9}$$

The velocity $v_{\max}$ that maximizes this Bartlett is selected as the phase velocity for that band and configuration, corresponding to the strongest overall phase coherence across the array. These velocities are subsequently used in the localization of real seismic sources and the synthetic uncertainty tests. A schematic overview of the complete MFP workflow and velocity estimation is provided in the Supplementary information (Text S1, Text S2)

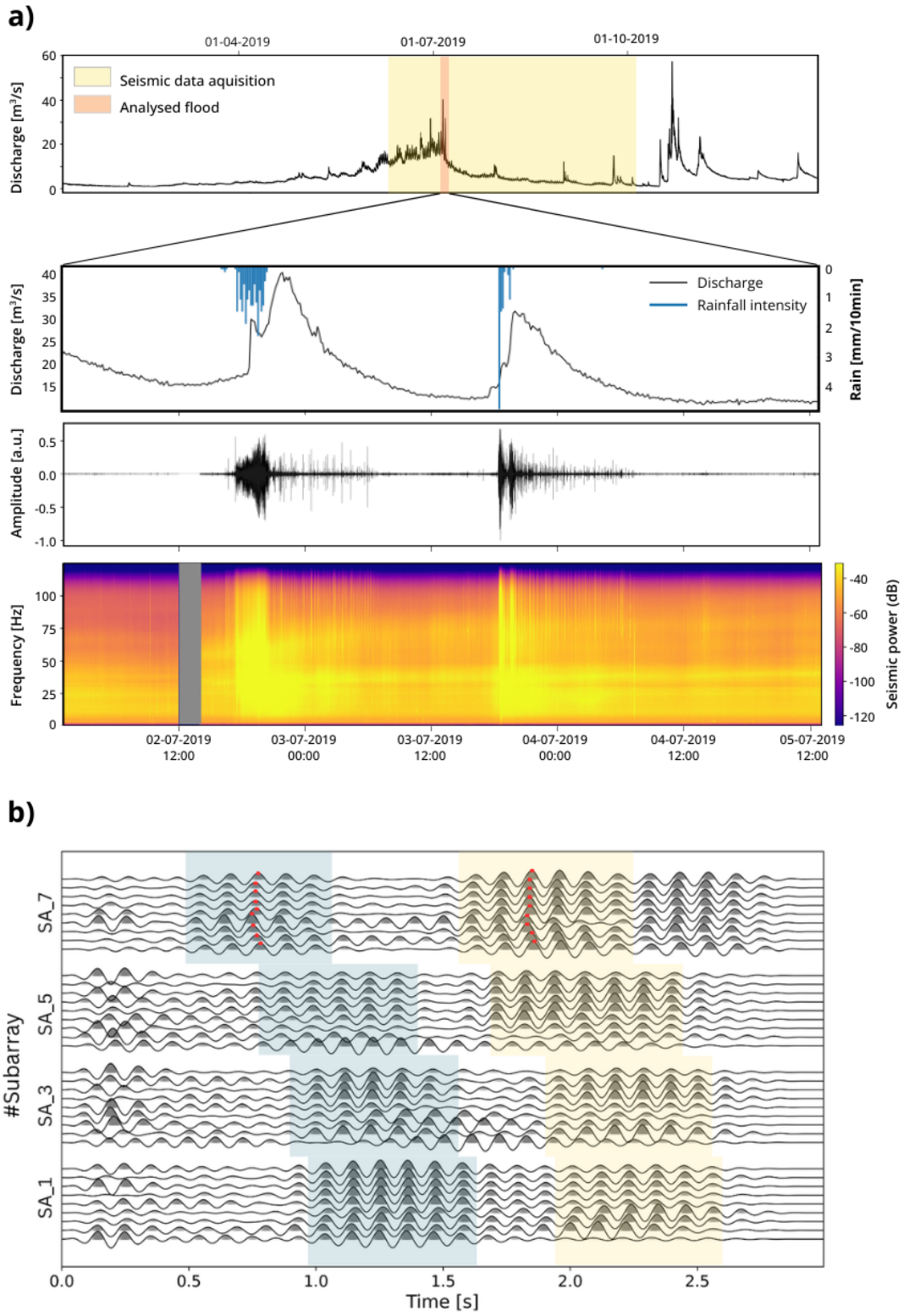


Figure 2 (a) Hydrological and seismic context of the July 2019 flood. Top: discharge record for 2019, highlighting the flood period (July 2–5). Middle: zoomed three-day record showing discharge and rainfall intensity. Lower panels: vertical-component seismogram and corresponding spectrogram at geophone 1, subarray 1. A short blank interval in the spectrogram corresponds to a period when sensors were under maintenance. (b) Filtered waveforms (10–15 Hz) across multiple subarrays showing short, coherent energy packets. Red dots mark the curvature of arrival times across sensors, indicating coherent wavefronts suitable for matched field processing.

3.2 Hybrid Strategy for Frequency-Resolved Source Localization

3.2.1 Principles

To capture a broad range of wavelengths given the fixed array geometry, we establish two approaches: *(i)* full-network processing, and *(ii)* subarray-averaged processing. Both approaches solve the Bartlett operator defined in equation (7), but differ in how the array aperture is used relative to the dominant wavelength. In the full-network processing approach, all sensors are used simultaneously to compute the MFP output $B(\mathbf{x}, c)$ over a three-dimensional search grid of horizontal coordinates $\mathbf{x} = (x, y)$ and phase velocity c. This strategy exploits the entire 500 m aperture and is suited for long wavelengths, for which equation (1) is satisfied.

In the subarray-averaged processing approach, the $B(\mathbf{x}, c)$ is first computed independently for each subarray using equation (7). Each subarray thus produces its own $B_i(x, y)$ map of coherence. These maps are then averaged spatially to obtain a single composite field,

$$B_{\text{avg}}(x, y) = \frac{1}{M} \sum_{i=1}^{M} B_i(x, y) \tag{10}$$

where M is the number of subarrays.

3.2.2 Synthetic Tests and Array Response

To evaluate the resolving power and directional sensitivity of the array as a function of frequency, we perform synthetic tests based on the array response. Here, the array response refers to the spatial coherence pattern produced by the MFP algorithm for a single, perfectly coherent source at a known location and frequency. It represents the theoretical best-case localization of the array, independent of noise or source complexity. We model the source time function as a time domain Ricker wavelet (Wang, 2015; Ricker, 1953), with zero-phase pulse defined as

$$s(t) = \left[1 - 2\pi^2 f_c^2 (t - t_0)^2\right] \exp\left[-\pi^2 f_c^2 (t - t_0)^2\right], \tag{11}$$

where $s(t)$ is the waveform amplitude at time t, f_c is the central (dominant) frequency, and t_0 is the time corresponding to the wavelet's center. Synthetic seismograms are generated at each sensor location by applying travel-time delays from a fixed source within the river channel, based on an assumed homogeneous velocity c, which is v_{max} in this case. The synthetic dataset is then processed using the same MFP formulation as in Section (3.1) to compute the array response function.

When the dominant wavelength λ exceeds or is comparable to the full-network aperture ($\lambda \gtrsim A_{\text{net}}$), the full network exhibits a sharply focused main lobe with weak sidelobes, indicating strong coherence across the entire array and stable localization (Figure 3a). As frequency increases and $\lambda \ll A_{\text{net}}$, the full-network response still peaks near the true source location in these noise-free synthetic tests, but develops numerous strong sidelobes. Although the true source is correctly identified, the presence of multiple sidelobes introduces ambiguity that would significantly degrade localization performance in the presence of noise. The opposite behaviour occurs in the subarray-averaged MFP (Figure 3b). At low frequencies, where $\lambda \gg A_{\text{sub}}$, the phase field is nearly identical for all trial locations and the Bartlett response becomes flat, reflecting a lack of resolving power. As frequency increases and $\lambda \gtrsim A_{\text{sub}}$, individual subarrays recover stable, well-defined beam patterns with reduced sidelobe interference, yielding more robust localization when coherence is restricted to subarray scales. For the Séveraisse array geometry considered here, this transition occurs at approximately 10 Hz, marking the frequency above which coherence becomes limited to subarray scales and subarray-based processing becomes necessary. In the following analyses we split the methodology by frequency: full-network processing is used at frequencies below 10 Hz where coherence spans the entire aperture, while subarray-based processing is applied at frequencies above 10 Hz where spatial coherence is limited to smaller scales.

3.3 Uncertainty Estimation

Accurate localization of seismic sources using MFP depends on signal coherence, signal-to-noise ratio (SNR), and array geometry. However, the MFP ambiguity surface itself does not provide a direct estimate of localization uncertainty. To quantify expected localization uncertainty as a function of frequency and source position, we develop a synthetic test framework.

We generate synthetic seismic sources at prescribed locations spanning the active river channel, using the same spatial grid and coordinate system as the real-data analysis. For each source location and frequency band, we construct synthetic waveforms using the source time function from equation (11) and progressively add noise to simulate real signals. We apply MFP to these synthetic datasets to evaluate how $B(\mathbf{x})$ changes with varying SNR, to obtain calibration curves between $B(\mathbf{x})_{\text{max}}$ and SNR. We map observed $B(\mathbf{x})$ from the real data onto these calibration curves to infer effective SNRs representative of the noise conditions under which real sources are detected. Subsequently we quantify uncertainty in localization as the distance between the true synthetic source location and the position of the maximum of the $B(\mathbf{x})$, averaged over multiple realizations. Full details of the synthetic source grid, waveform generation, noise model, and calibration procedure are provided in the Supplementary Information (Text S3).

3.4 Timelapse Image Processing and Orthorectification

To compare the timelapse images quantitatively with seismic source locations, oblique raw photographs must be (i) georeferenced, meaning assigned real-world coordinates, and (ii) orthorectified, meaning corrected for perspective and terrain-induced distortion so that distances and shapes are spatially accurate. The camera captured oblique images of the study reach (Figure 4a, b). We use the Georeferencer tool in QGIS together with a 0.06 m resolution digital elevation model

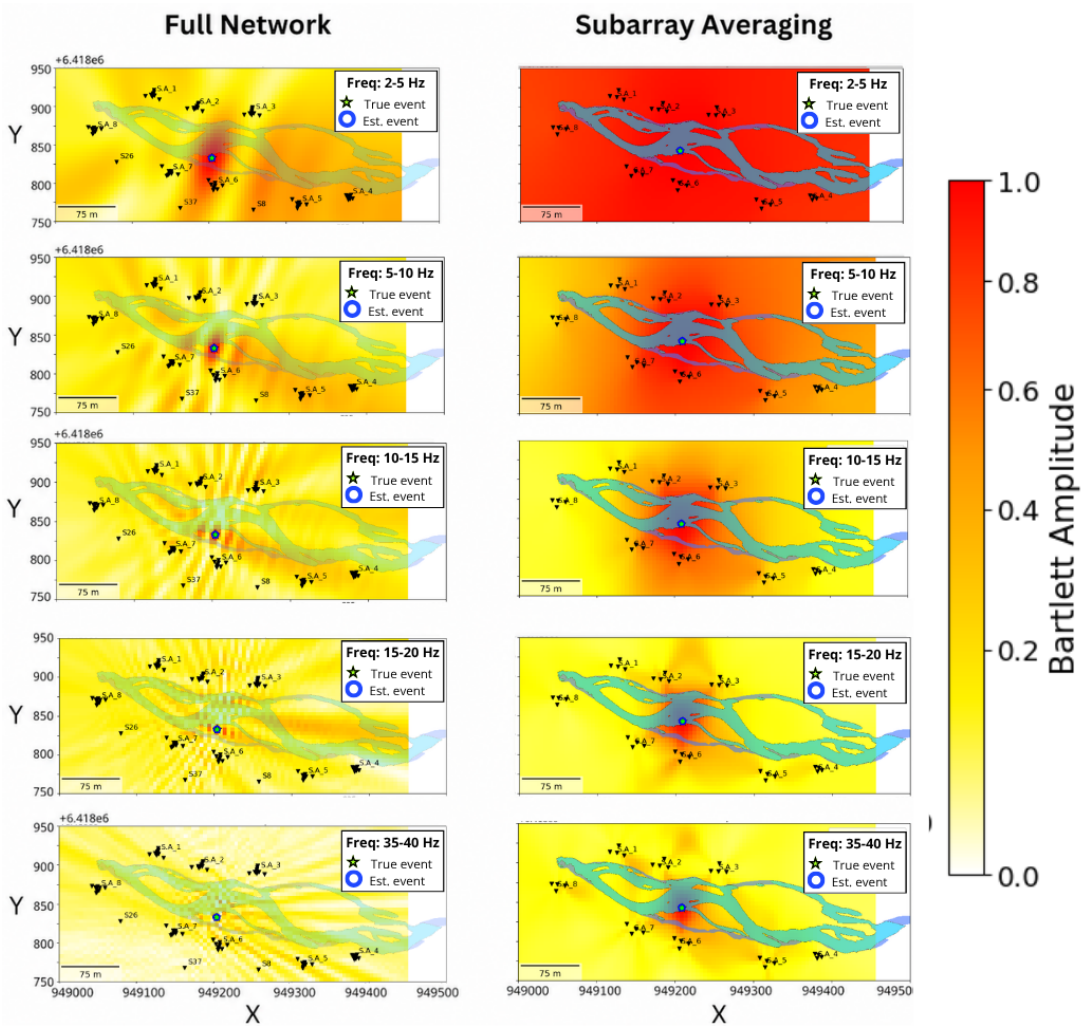


Figure 3 Comparison of array response maps computed using the full network (left column) and the subarray-averaged configuration (right column). From top to bottom, rows correspond to the frequency bands 2–5 Hz, 5–10 Hz, 10–15 Hz, 15–20 Hz, and 35–40 Hz. The colorscale represents normalized Bartlett amplitude, with warmer colors indicating higher phase coherence. Stars indicate the true source location, while open blue circles indicate the estimated source location.

(DEM) derived from drone surveys acquired at several time steps during the study period. We select stationary, easily identifiable features visible in both the oblique photographs and the DEM, such as large boulders, bar margins, and isolated trees, which are used as ground control points (GCPs). We extract their plan-view coordinates from the DEM and manually match to the corresponding pixel locations in each image (Figure 4e). We use the Projective transformation algorithm in the georeferencer tool, which corrects for perspective distortion associated with oblique viewing geometry while preserving straight lines. Although a minimum of four GCPs is required, we use 12 GCPs distributed across the visible channel to ensure accurate correction over the entire field of view. This procedure yields orthorectified, georeferenced GeoTIFF images in the Lambert-93 coordinate system (Figure 4c).

Following orthorectification, we extract the wetted channel from each image using RGB thresholding (Figure 4d). Threshold values are manually adjusted to account for variations in illumination and shadowing. The resulting binary masks are refined using morphological filtering to remove isolated artefacts and to ensure continuous channel boundaries. We use these processed channel outlines to interpret the seismic source density maps and assess whether clusters of seismic energy coincided with specific braids, bar margins, or zones of morphological change.

4 Results

4.1 Frequency-Dependent Phase Velocity Estimation

We invert phase velocities from MFP outputs for each frequency band by identifying the phase velocity that maximises the Bartlett amplitudes. For this purpose, we apply MFP to a set of coherent seismic sources recorded during the main flood period, and the Bartlett amplitude is evaluated over a range of trial phase velocities to obtain the Bartlett amplitude as a function of velocity (see Supplementary Information Text S2 for details).

The dispersion curves obtained from this MFP-based velocity estimation exhibit a systematic decrease in phase velocity with increasing frequency (Figure 5a), consistent with higher-frequency surface waves sam-

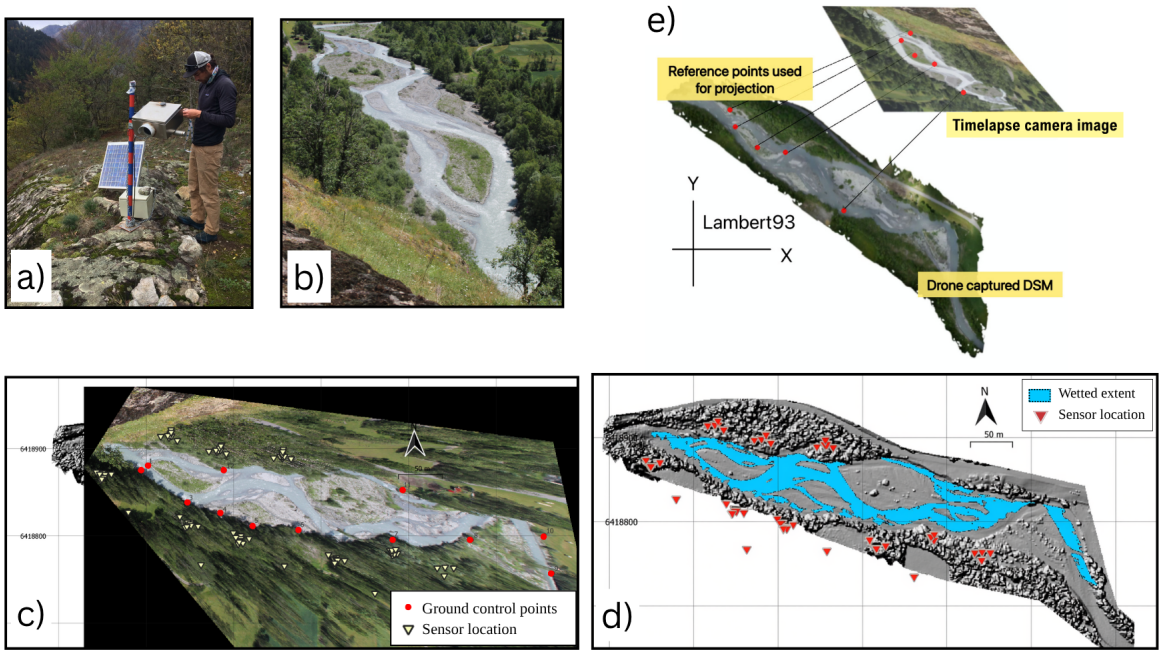


Figure 4 Overview of the timelapse image processing workflow used for orthorectification and channel extraction. (a) Downstream fixed-position timelapse camera overlooking the study reach (installed 64 m above the river, azimuth $\sim 298°$). (b) Raw oblique RGB image captured during the flood. (c) Orthorectified and georeferenced image (Lambert-93) produced using a 0.06 m DEM and GCPs. (d) Extracted wetted channel obtained from RGB thresholding, shown overlaid on the DEM. (e) Schematic illustration of the orthorectification process: ground control points (GCPs) identified in both the DEM and oblique image define the projective transformation that maps the photograph into plan-view coordinates.

pling shallower and less consolidated materials. Over the investigated frequency range, seismic wave velocity is approximated by a power-law relation $v(f) = v_{p0}\, f^{-\xi}$ with best-fitting parameters $v_{p0} \approx 1055\ \mathrm{m\,s^{-1}}$ and $\xi \approx 0.40$. Phase velocity is less well constrained at frequencies approaching the practical limits of the respective array configurations (Supplementary Information Text S2). Sensitivity tests around these less well-constrained velocities produce some variation in the detailed source-density distributions, but preserve their first-order spatial organisation (Figure S2.3). For comparison, Figure 5a also shows empirical phase-velocity scalings proposed by Bakker et al. (2022), derived from active rock-drop experiments conducted on the same Séveraisse River, and by Tsai et al. (2012) for generic bedrock settings. Bakker et al. (2020) reported a scaling of the form $v(f) = 680\, f^{-0.31}$, while Tsai et al. (2012) proposed $v(f) = 1295\, f^{-0.39}$. The dispersion trend obtained here is broadly consistent with the exponent reported by Tsai et al. (2012) and somewhat steeper than that inferred by Bakker et al. (2020). Differences in prefactor and exponent likely reflect a combination of spatial sampling effects, as the active-source velocities of Bakker et al. (2020) were primarily evaluated within the floodplain, as well as the integration of heterogeneous near-surface materials and mixed source processes in the passive wavefield. The prefactor v_{p0} obtained here lies between values reported for shallow sedimentary layers and generic bedrock references, consistent with the mixed geological conditions of the Séveraisse braided reach.

4.2 Seismic Source Localisation and Spatial Clustering

Figure 5b shows the maximum Bartlett amplitudes obtained from the systematic MFP analysis as a function of frequency. The Bartlett-amplitude distributions differ between the two processing approaches; therefore, we define the retention criterion — the criterion to define the source, separately for the two frequency ranges. Below 10 Hz, full-network MFP requires phase consistency across the entire array aperture and generally produces lower maximum Bartlett amplitudes and hence we retain windows with maximum Bartlett amplitudes above the mean of the corresponding frequency-band distribution. Above 10 Hz, the analysis is based on spatially averaged subarray responses, for which coherence is preserved over the smaller subarray apertures and the resulting Bartlett values are systematically higher and we use a more conservative mean $+1\sigma$ criterion. For each 3 s window, the position of the maximum Bartlett amplitude is retained as an accepted source location only when it exceeds the corresponding criterion. As different retention criteria are used below and above 10 Hz, we do not interpret differences in the absolute number or density of accepted source locations quantitatively across frequency bands, but instead focus on their first-order spatial organisation.

Figure 6 shows source density maps constructed from these accepted source locations during the peak flood interval from 21:30 to 22:30 on July 2, corresponding to an average discharge of 39.02 $\mathrm{m^3\ s^{-1}}$. The maps are shown for representative frequency bands of 5–10, 15–20, 25–30, and 30–35 Hz. The lower panel displays

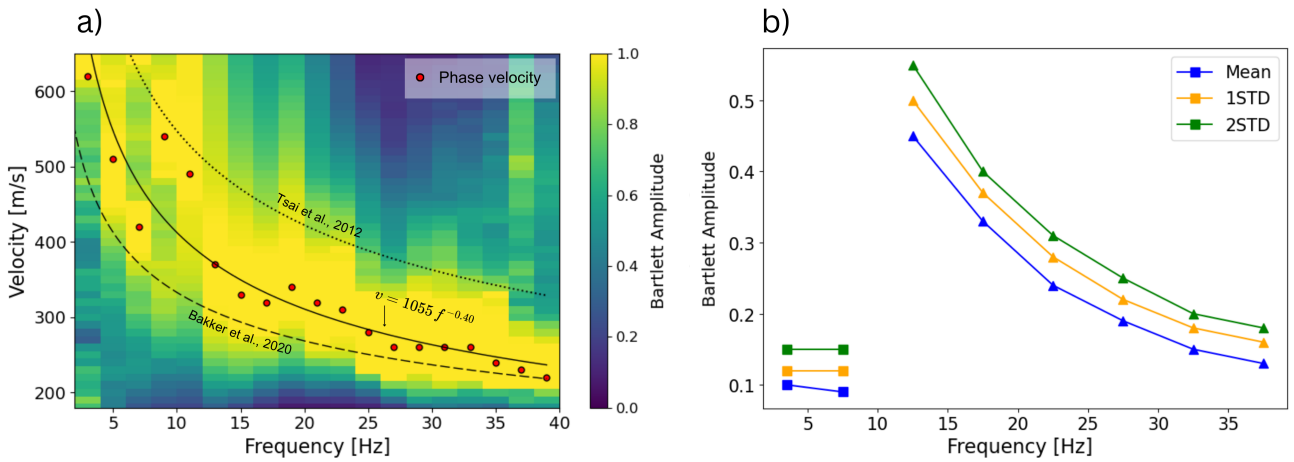


Figure 5 a) Phase velocity estimated from matched field processing (MFP). The colormap indicates the Bartlett amplitude normalized within each frequency range. Red circles denote the phase velocity $v_{\max}(f)$ that maximizes Bartlett amplitude within each frequency band. The solid black line shows a power-law fit to the MFP-derived dispersion, $v(f) = 1055 f^{-0.40}$. Dashed and dotted lines indicate phase-velocity scalings proposed by Bakker et al. (2020), derived from active rock-drop experiments on the Séveraisse River, and by Tsai et al. (2012) for generic bedrock settings. b) Frequency-dependent Bartlett amplitude statistics derived from one hour of continuous data. Curves show the mean, mean $+1\sigma$, and mean $+2\sigma$ of the Bartlett-amplitude distributions within each frequency band. Squares denote results obtained using full-network MFP (2–10 Hz), whereas triangles denote results obtained using subarray-averaged MFP (10–40 Hz)

the discharge evolution from the evening of July 2 to the evening of July 3, with the analyzed one-hour flood peak interval highlighted. Across all frequency bands, sources are spatially confined to the active river channel, indicating that coherent seismic energy originates predominantly within the channel rather than from off-channel sources. However, their spatial organisation varies with frequency. The 5–10 Hz band exhibits a broader, channel-wide source distribution, whereas the higher-frequency bands (15–35 Hz) exhibit more compact and spatially clustered source regions

4.3 Uncertainty Estimation

We quantify uncertainty in source locations using synthetic tests. Effective signal-to-noise ratios (SNRs) for real detections were inferred by comparison with synthetic simulations, allowing uncertainty to be evaluated under noise conditions representative of the observations (see Section 3.3 and Supplementary Information Text S3). For each synthetic source, we estimate the SNR value that yields a Bartlett amplitude matching the observed value; this defines an equivalent SNR field (Figure 7a, b). At low frequencies (5–10 Hz, panel a), equivalent SNRs are relatively high and spatially homogeneous (approximately -11 to -13.5 dB), whereas at higher frequencies (30–35 Hz, panel b) SNR values are lower and more spatially variable (approximately -15 to -26 dB), reflecting reduced phase coherence and shorter coherence lengths. The corresponding localization uncertainty maps derived from the synthetic tests are shown in Figure 7c, d. At 5–10 Hz (panel c), uncertainty varies from 5 to 30 m and is lowest near the dense sensor clusters. At 30–35 Hz (panel d), uncertainties increase to 10–140 m and become spatially heterogeneous due to reduced coherence and limited aperture of individual subarrays. Mean absolute uncertainty remains below ∼6 m for 2–5 Hz and ∼4.2 m for 5–10 Hz, within 10 m for 10–30 Hz, and increases to approximately 35 m at 30–35 Hz and 100 m at 35–40 Hz (Figure 9a). Normalizing localization uncertainty by wavelength (U/λ) reveals that sub-wavelength resolution ($U/\lambda < 1$) is achieved for frequencies below 30 Hz. In this regime, a sufficient number of sensors record mutually consistent phase delays, allowing the Bartlett output to form a stable and well-defined maximum. Above 35 Hz (Figure 9b), U/λ increases rapidly, exceeding ∼15 wavelengths, indicating that phase coherence is no longer maintained across the array or even within individual subarrays. In this regime, the beamformer output becomes fragmented with multiple competing maxima, consistent with reduced inter-sensor phase coherence and limited effective aperture at high frequencies. Such coherence loss may be further enhanced by frequency-dependent attenuation and scattering, although these effects are not explicitly represented in our synthetic tests.

5 Discussion

5.1 Hybrid Localization Strategy for Frequency-dependent Analysis

The hybrid use of dense array network into full-network and subarray-averaged MFP enables robust localization across a wide frequency range. At low frequencies (2–10 Hz), where wavelengths exceed the inter-station spacing and coherence extends across the full aperture ($\lambda \gtrsim A_{\text{net}}$), full-network MFP provides stable and sharply focused maxima. However, at higher frequencies, coherence is lost across the large array, and full-network MFP yields broad ambiguity surfaces with strong sidelobes (Figure 3). By contrast, the subarray-averaged approach maintains coherence within smaller

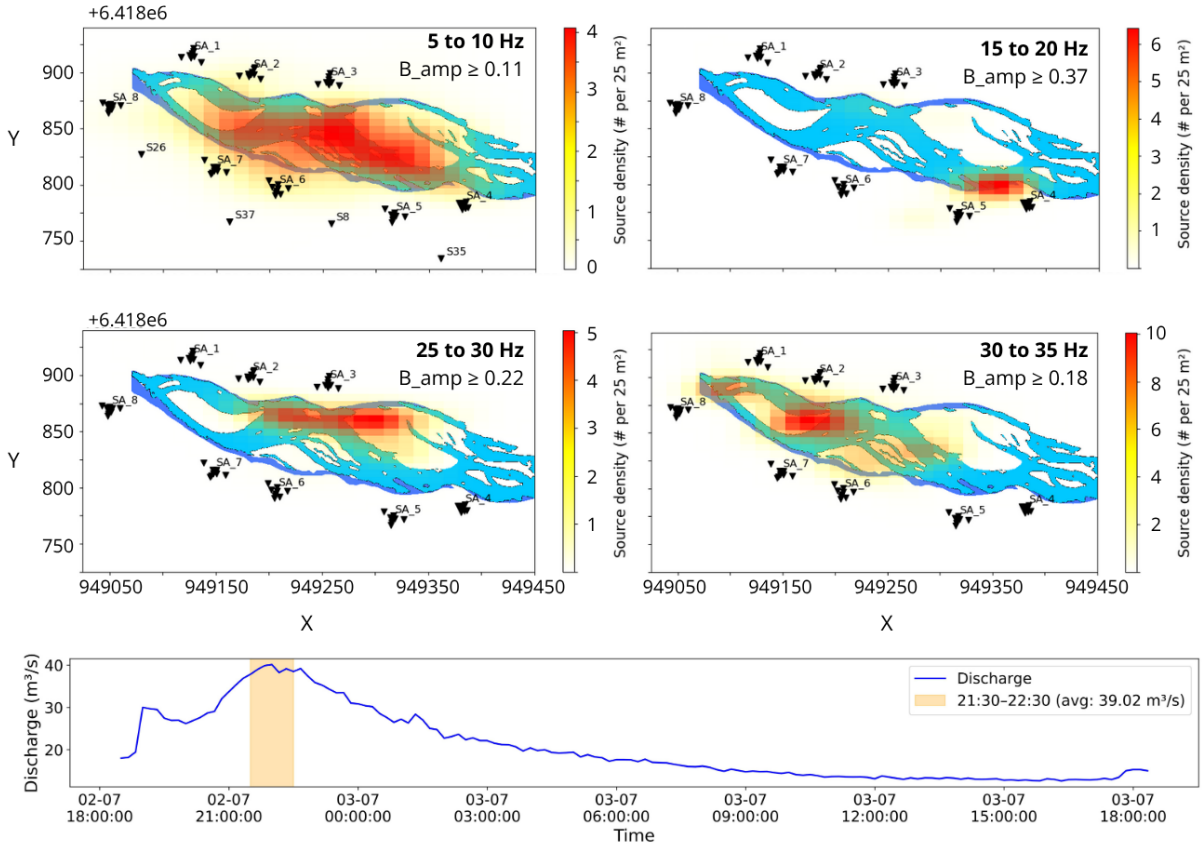


Figure 6 Hourly seismic source-density maps for the period 21:30–22:30 on July 2, corresponding to the peak flood interval (average discharge: 39.02 $m^3\ s^{-1}$). Source locations are projected in plan view over the study reach, with density indicating the number of accepted source locations per grid cell during the one-hour interval. The bottom panel shows the discharge time series over July 2–3, with the shaded rectangle indicating the one-hour interval represented in the source-density maps.

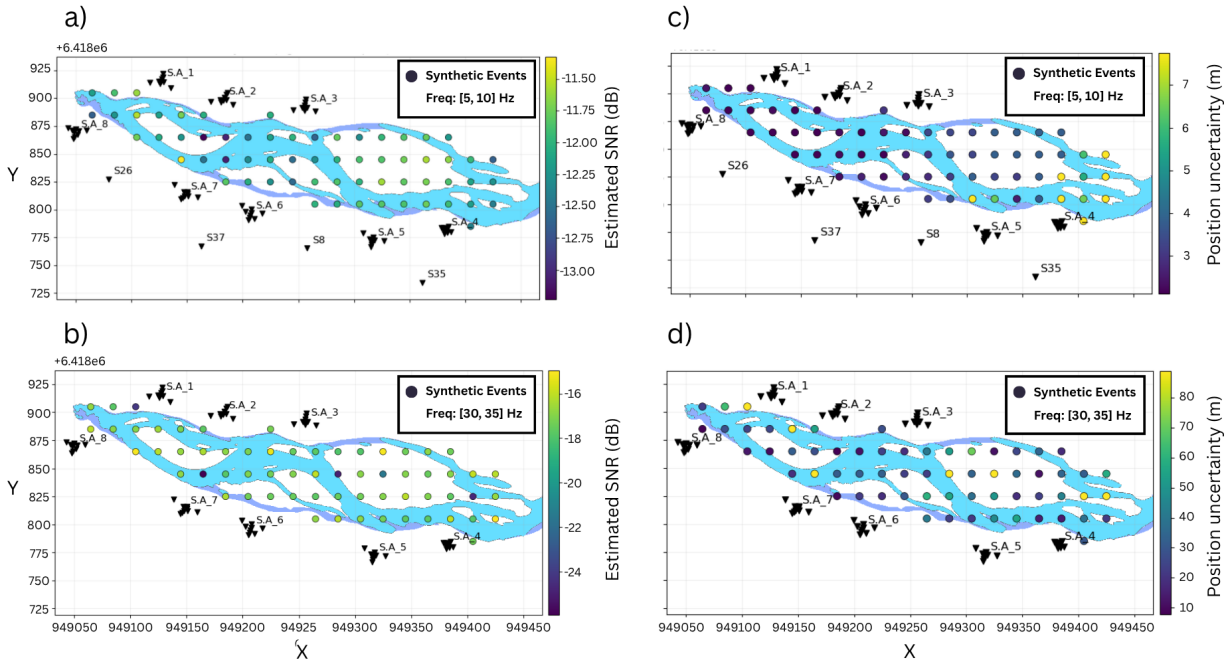


Figure 7 (a, b) Equivalent SNR distributions estimated for real sources by matching observed Bartlett amplitudes to synthetic calibration curves: (a) 5–10 Hz and (b) 30–35 Hz. (c, d) Corresponding localization uncertainty maps computed from synthetic tests at each location and frequency band. At low frequencies, uncertainty remains small (5–30 m), while at high frequencies it increases (10–140 m) and becomes spatially heterogeneous.

apertures, producing reliable localization results up to 30 Hz. Although one could in principle perform full-array MFP at all frequencies by imposing a fixed phase velocity, such an approach leads to significant sidelobe contamination and ambiguous source maps (see Figure 3). Subarray averaging mitigates these issues while retaining sensitivity to near-field sources through the use of curved wavefronts rather than plane-wave assumptions.

Conceptually, this hybrid strategy allows dense seismic arrays to operate as multi-scale observatories, resolving both broad, low-frequency sources and fine, high-frequency processes within the same dataset. In the far-field limit, where sources are distant relative to subarray aperture, a plane-wave beamforming approach applied independently to subarrays and analyzed through azimuthal distributions would be expected to yield similar localization trends. The present MFP-based framework, however, naturally exploits the curvature of the wavefield and therefore retains sensitivity to near-field sources, providing a unified approach that remains valid across a wider range of source distances and frequency regimes.

5.2 Frequency-dependent Source Distributions and Physical Interpretation

The source density maps (Section 4.2) reveal consistent spatial patterns throughout the study period. All sources remain confined to the active river channel, confirming that the dominant seismic energy originates from fluvial processes rather than anthropogenic or off-channel noise. The spatial distribution of seismic sources exhibits a distinct frequency dependence that is consistent with changing relative contributions of fluid-driven and sediment-related processes.

At low frequencies (2–5 Hz), the seismic source distributions are broad and diffuse, spanning the majority of the channel width (Figure 6). This pattern is consistent with energy generated by turbulent flow and pressure fluctuations acting over extended regions of the bed (Gimbert et al., 2014; Coviello et al., 2015). During high-flow stages, coherent vortical structures and bed shear stresses act across the full wetted width of the braided channel, creating distributed excitation. Because the observed spatial extent of these sources (tens of meters) significantly exceeds the localization uncertainty for this band ($\sim \lambda/10$, or $<$10 m), we expect the source distribution to reflect genuinely distributed energy generation rather than a methodological artifact. At higher frequencies (10–40 Hz), source locations become more spatially heterogeneous and form more compact clusters within the active channel. While sources at 10–15 Hz appear most spatially compact, at frequencies above $\sim$ 30 Hz the sources become more spatially scattered along the channel. This transition could be due to two factors: first, as frequency increases, the wavelength shortens, and the spatial coherence of the wavefield decreases, so that fewer sensors share mutually consistent phase delays. In practice, coherent signals may be recorded only within individual subarrays, which can favour slightly different source locations and produce multiple competing maxima in the beamformer output. Second, the physical signal itself being created by finer sediment of low-energy occurring in various places due to en masse motion across broader areas. Previous observational and theoretical studies associate higher-frequency river seismic energy as preferentially generated by sediment transport (Schmandt et al., 2013; Gimbert et al., 2014; Bakker et al., 2020). The more localized nature of sources at higher frequencies attributed to bedload is consistent with expectations of bedload transport being intermittent and localized in spatially concentrated patches even under relatively uniform hydraulic forcing as a result of local destabilizations (Lajeunesse et al., 2010; Piantini et al., 2021). Spatial variations in flow conditions, bed structure, and sediment availability across the braided Séveraisse reach are likely to further enhance this heterogeneity (Recking et al., 2024).

Localization remains at sub-wavelength scales up to about 25 Hz (uncertainty $< 4\lambda/5$). Beyond $\sim$35 Hz, however, localization uncertainty exceeds one wavelength, and hence the source locations inferred in this frequency range should therefore be interpreted with caution.

Figure 8 provides qualitative hydraulic context for these frequency-dependent patterns. Panel (a), acquired shortly before the flood peak, shows a partially confined flow concentrated within the main braids. Panel (b), acquired immediately after peak discharge, reveals a visibly expanded wetted area, particularly within the region enclosed by the dashed green outline. This expansion corresponds to zones of flow spreading across the braid plain, where flow deceleration and preferential deposition are expected. The spatial extent of this inundated region corresponds to the broad low-frequency (2–5 Hz) source distribution, consistent with distributed hydraulic forcing across the expanded wetted area. At higher frequencies (15–35 Hz), the dominant source regions are associated with major braids, confluences, bifurcation points, and zones of concentrated flow. Sources in the 25–35 Hz frequency range (region enclosed by red and blue dashed lines) are concentrated within well-defined flow paths, often corresponding to the outer sides of channel bends (extrados) and zones of flow concentration, where sediment grains are expected to experience stronger accelerations and more energetic impacts. This spatial partitioning is consistent with a low-frequency wavefield dominated by more spatially distributed hydraulic forcing, while the higher-frequency source regions are compatible with a stronger contribution from spatially heterogeneous sediment-transport processes within the active channel.

5.3 Array Design and Recommendations for Future Experiments

5.3.1 Sensitivity of Localization Uncertainty to Sensor Density and Array Aperture

We assess how localization accuracy depends on array configuration using two array-degradation experiments to isolate the roles of sensor density and array

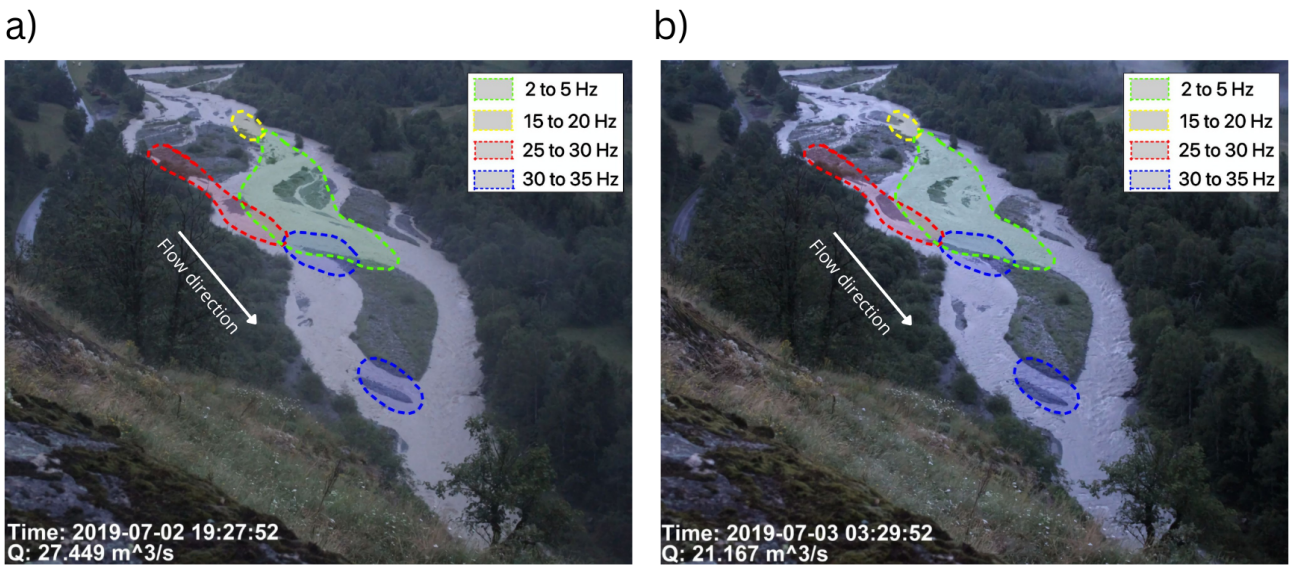


Figure 8 Timelapse images of the Séveraisse River reach acquired (a) at 19:27 on July 2 (just before flood peak) and (b) at 03:29 on July 3 (immediately after peak flow). Dashed outlines indicate regions of dominant seismic source activity identified in different frequency bands: 2–5 Hz (green), 15–20 Hz (yellow), 25–30 Hz (red), and 30–35 Hz (blue).

aperture. In the first experiment (sensor reduction), we progressively remove sensors within each subarray while keeping the number and spatial distribution of subarrays fixed. In the second experiment (subarray reduction), we remove entire subarrays from the network while preserving the internal geometry of the remaining subarrays, thereby reducing the effective aperture and azimuthal coverage of the array. For both experiments, we perform multiple random realizations of sensor or subarray removal to minimize spatial bias. These two tests independently quantify the influence of local sensor density (N) and total array aperture (M) on localization performance respectively. At low frequencies (2–10 Hz), where we apply full-network MFP, uncertainties remain low under sensor reduction (Figure 9c). Uncertainty for 2–5 Hz ($\lambda \sim 150$ m) ranges from 0.04–0.08λ (6–11 m), while for 5–10 Hz ($\lambda \sim 64$ m) it remains below 0.2λ (~ 13 m). These sub-wavelength values indicate super-resolved performance, reflecting the strong phase coherence and large aperture achieved under full-network processing, even when the sensor density is compromised. In contrast, subarray removal (Figure 9d) causes an order-of-magnitude increase in uncertainty, from 0.05λ (8 subarrays) to 1–2λ with only one subarray. This reflects the dominant role of aperture in preserving azimuthal coverage at low frequencies. At high frequencies (10–40 Hz), where we apply subarray-averaged MFP, similar patterns emerge but with stronger frequency dependence (Figures 9). Below 25 Hz, uncertainties remain below one wavelength for configurations with at least 7 sensors and 7 subarrays. Above 25 Hz, uncertainties increase rapidly, with $U > 20\lambda$ at 35–40 Hz, even under full geometry.

This provides practical guidance for array design. When sensor availability is limited, distributing sensors across more subarrays improves performance more than densifying individual subarrays. For the current network geometry, MFP-based localization is reliable up to 30 Hz; beyond this range, reduced phase coherence limits the applicability of phase-based methods, and alternative localization strategies may be more appropriate

5.3.2 Effect of Lateral Asymmetry

To evaluate the impact of uneven spatial coverage, we test scenarios where all subarrays on one riverbank are removed, creating a laterally asymmetric array. This configuration simulates field constraints where access is limited to a single bank. The full network consisted of eight subarrays: five on the left bank (Subarrays 4–8) and three on the right bank (Subarrays 1–3). We compare uncertainties for the following scenarios: full network, left-bank removal, and right-bank removal.

At low frequencies (2–10 Hz), removing one bank significantly degraded performance. In the 2–5 Hz band, normalized uncertainty increased from 0.04λ (full) to 0.76λ (right-bank removal) and 1.45λ (left-bank removal), with relative penalties up to 19$\times$ (Figure 9e, f). This reflects the loss of azimuthal aperture and the collapse of the 2D array geometry into a linear array. In the 10–25 Hz range, uncertainty remained within 1–2 wavelengths across configurations, but increased by factors of 1.5–5 under asymmetry. Removal of left bank sensors, which contribute to a larger aperture, impose consistently greater penalties. Above 25 Hz, uncertainty exceedes 5–15λ even with the full array, due to short wavelengths and coherence loss. Lateral asymmetry introduces only marginal increases (1.2–2.5$\times$), indicating that geometry had limited influence in this resolution-limited regime. This suggests that having sensors on both banks is essential for robust localization below 10 Hz. In the mid-frequency band (10–25 Hz), localization remains feasible under asymmetric deployments, but with reduced accuracy. At higher frequencies, where resolution is governed by wavelength rather than geometry, additional array asymmetry has minimal effect.

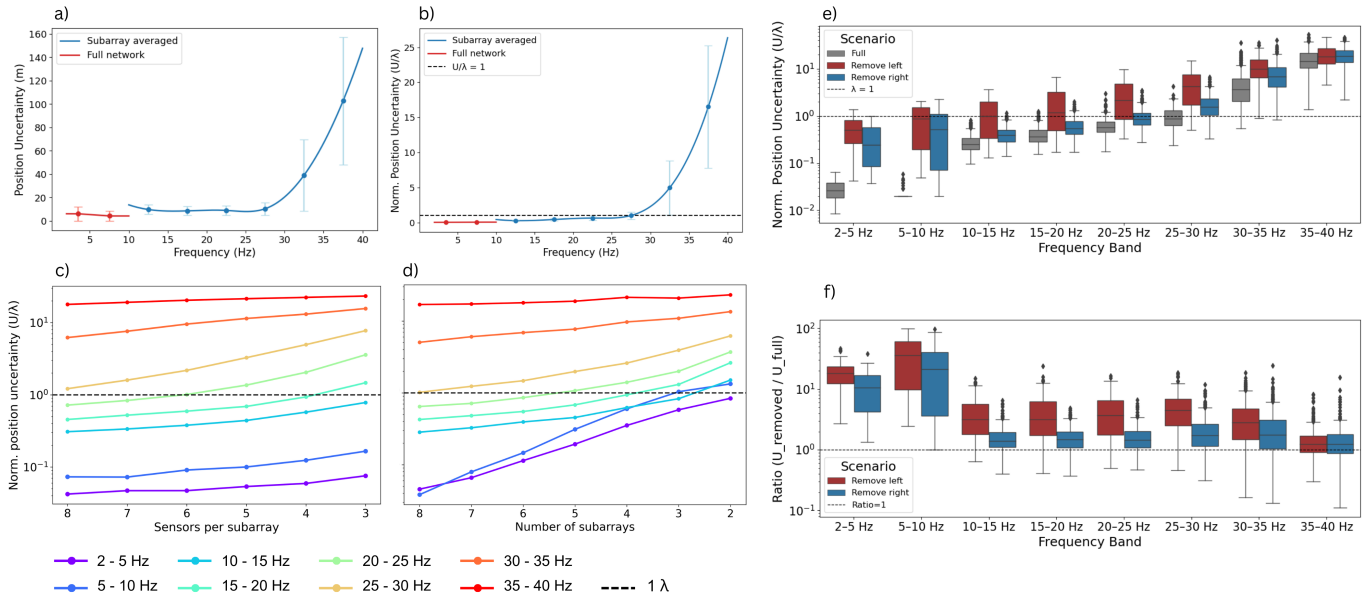


Figure 9 Localization uncertainty from synthetic MFP tests. (a) Mean absolute uncertainty and (b) wavelength-normalized uncertainty as a function of frequency. Red: full-network (2–10 Hz); blue: subarray-averaged (10–40 Hz). Error bars denote one standard deviation among all simulated events c)Wavelength-normalized localization uncertainty (U/λ) as a function of the number of sensors per subarray and d) the number of subarrays. Horizontal dashed lines indicate the $U/\lambda = 1$, an uncertainty of one wavelength.
(e)-(f): Effect of lateral asymmetry on localization accuracy. e)Wavelength-normalized localization uncertainty (U/λ) across frequency bands, shown as boxplots for full (gray), left-bank removed (red), and right-bank removed (blue) configurations. Uncertainty increases sharply at low frequencies under asymmetric deployments. f)Relative uncertainty penalty ($U_{\mathrm{removed}}/U_{\mathrm{full}}$) as a function of frequency. Penalties exceed 10–40$\times$ below 10 Hz, particularly when removing the left bank (red), which contained more subarrays.

Design Parameter	Guideline / Recommendation
Processing Mode	Select processing mode based on the wavelength-to-aperture ratio. Use *full-network MFP* when the dominant wavelength satisfies $\lambda \gtrsim A_{\mathrm{net}}$, indicating coherence across the entire array. Apply *subarray-averaged MFP* when $\lambda \lesssim A_{\mathrm{net}}$ but $\lambda \gtrsim A_{\mathrm{sub}}$, such that coherence is maintained within subarrays but lost across the network.
Sensor Spacing	Ensure inter-station spacing $\Delta l \leq \lambda/2$ to avoid aliasing. A more conservative spacing criterion, $\Delta l \leq \lambda/3$, has been suggested in highly scattering near-surface environments to reduce aliasing and improve stability (Wathelet et al., 2008).
Array Aperture	Maintain a total network aperture A_{net} at least several wavelengths across the target dimension to ensure directional resolution. For low frequencies (long λ), prioritize inter-subarray spacing and lateral coverage; for high frequencies (short λ), favor smaller subarray apertures to preserve coherence.
Subarray Size and Sensor Density	Deploy at least five sensors per subarray to maintain intra-subarray coherence ($A_{\mathrm{sub}} \lesssim \lambda$). Beyond six sensors per subarray, further gains in accuracy are minor. For 15–25 Hz under typical river conditions ($c \approx$ 400–600 m/s), this corresponds to subarray apertures of 20–25 m.
Lateral Symmetry	Ensure bank-to-bank coverage to preserve azimuthal symmetry. Removing one riverbank increases localization uncertainty by up to $40\times$ at low frequencies (2–5 Hz); thus, two-bank deployment is essential whenever λ exceeds the channel width.

Table 1 Design guidelines for dense seismic arrays in frequency-resolved environmental source localization.

5.3.3 Instrument Deployment Strategies

Localization accuracy depends strongly on array geometry and frequency, emphasizing the need to tailor deployment strategies to the dominant signal types. Table 1 compiles the array design guidelines inferred from this study.

These deployment principles provide a generalizable framework for future environmental seismic experiments. They emphasize that sub-wavelength resolution is achievable without extreme sensor densities, provided that array geometry spans the active source region. In complex field settings where two-bank coverage is infeasible, localization performance can still be optimized by favoring spatial aperture. These insights are broadly applicable to other monitoring contexts involving broadband, spatially distributed sources, including glacier dynamics and hillslope processes.

6 Conclusion

We establish a generalized framework for frequency-resolved seismic source localization in fluvial environments using dense seismic arrays. Building on Matched Field Processing, we develop a hybrid localization strategy that adapts array configuration to frequency-dependent coherence, combining full-network MFP at low frequencies with subarray-averaged MFP at higher frequencies. This approach resolves the broad spectrum of river-generated seismic sources, from spatially distributed turbulence to localized bedload impacts, within a single, coherent observational framework.

Applied to one hour of continuous seismic data from the Séveraisse River during the July 2019 flood, the method reveals systematic differences in source organization across the 2–40 Hz frequency range. Low-frequency sources are spatially broad and extend over substantial portions of the active channel, consistent with spatially distributed hydraulic forcing associated with turbulent flow and pressure fluctuations. At intermediate frequencies, source locations become more spatially heterogeneous and form compact clusters within particular braids, confluences, bifurcations, and zones of concentrated flow. We interpret these higher-frequency patterns as being consistent with spatially heterogeneous sediment-transport activity when considered together with their frequency content, hydraulic setting, and previous observations of sediment transport at the Séveraisse.

Synthetic tests quantify localization accuracy as a function of frequency, signal-to-noise ratio, and array geometry. Expressed relative to channel geometry, uncertainties remain below 2% of the channel length and approximately 12% of the channel width for frequencies below 30 Hz. These values indicate that the observed frequency-dependent spatial patterns resolve features at the scale of hydraulic units within the braid plain, confirming that the mapped source distributions reflect genuine process partitioning rather than methodological artifacts. Array-degradation tests demonstrate that localization accuracy is primarily controlled by array aperture rather than local sensor density. Reducing the number of subarrays imposes substantially larger penalties than thinning sensors within subarrays, particularly at low frequencies where broad azimuthal coverage is essential. Removing one riverbank increases uncertainty by more than an order of magnitude, highlighting the importance of lateral symmetry for preserving coherence.

Beyond methodological advances, this study highlights the potential of dense array seismology to observe flood-driven geomorphic processes. While we focus here on a short flood interval, extending this approach to longer time series may reveal persistent or transient seismic sources associated with evolving channel states. Low-frequency seismicity may inform reach-scale flow dynamics, while higher-frequency signals can constrain the timing and location of bedload-dominated transport. Integration with complementary observations such as timelapse imagery, tracer experiments, or hydrodynamic models offers a promising path toward a more complete characterization of fluvial morphodynamics.

Overall, through this work we provide a physically grounded and field-tested framework for broadband seismic source tracking in rivers. By explicitly accounting for frequency-dependent coherence and uncertainty, it establishes a scalable foundation for monitoring complex surface processes in fluvial, glacial, and other geomorphic environments.

Acknowledgements

This work was supported by the Horizon Europe Marie Skłodowska-Curie Doctoral Network EnvSeis (Grant Agreement No. 101073148), which funded Samidha Revankar, and by the ANR project SEISMORIV (ANR-17-CE01-0008) granted to Florent Gimbert. The authors thank Adrien Gilbert and Benoît Urruty for their assistance during field operations and the installation of the dense seismic array. We also thank Adèle Johannot and Firmin Fontaine for the installation and maintenance of the timelapse camera system, as well as for providing the timelapse imagery used in the analysis.

Data and code availability

The seismic dataset used in this study, including the dense array recordings compiled into MATLAB (.mat) file containing station coordinates and waveform data arrays, as well as the code used for the matched field processing (MFP) computations, are available in the Zenodo repository (https://doi.org/10.5281/zenodo.18887672). River discharge data were obtained from the Mendeley Data repository (Misset et al. 2020b; http://dx.doi.org/10.17632/nxvhnjmg8j.1). Supplemental information accompanying this article provides additional methodological details and supporting analyses.

Competing interests

The authors declare no competing interests.

References

Ali, H. K. and Bean, C. J. Source location and wavefield characterization of river-induced seismic tremor. 2022. doi: 10.31223/X51P91.

Almendros, J., Ibáñez, J. M., Alguacil, G., and Del Pezzo, E. Array analysis using circular-wave-front geometry: an application to locate the nearby seismo-volcanic source. *Geophysical Journal International*, 136(1):159–170, 1999. doi: 10.1046/j.1365-246X.1999.00699.x.

Baggeroer, A. B., Kuperman, W. A., and Mikhalevsky, P. N. An overview of matched field methods in ocean acoustics. *IEEE Journal of Oceanic Engineering*, 18(4):401–424, 2002. doi: 10.1109/48.262292.

Bakker, M., Gimbert, F., Geay, T., Misset, C., Zanker, S., and Recking, A. Field Application and Validation of a Seismic Bedload Transport Model. *Journal of Geophysical Research: Earth Surface*, 125 (5):e2019JF005416, May 2020. doi: 10.1029/2019JF005416.

Bakker, M., Legout, C., Gimbert, F., Nord, G., Boudevillain, B., and Freche, G. Seismic modelling and observations of rainfall. *Journal of Hydrology*, 610:127812, 2022. doi: 10.1016/j.jhydrol.2022.127812.

Bertoldi, W., Zanoni, L., and Tubino, M. Assessment of morphological changes induced by flow and flood pulses in a gravel bed braided river: The Tagliamento River (Italy). *Geomorphology*, 114(3):348–360, 2010. doi: 10.1016/j.geomorph.2009.07.017.

Burtin, A., Bollinger, L., Vergne, J., Cattin, R., and Nábělek, J. L. Spectral Analysis of Seismic Noise Induced by Rivers: A New Tool to Monitor Spatiotemporal Changes in Stream Hydrodynamics. *Journal of Geophysical Research: Solid Earth*, 113(B5): 2007JB005034, May 2008. doi: 10.1029/2007JB005034.

Burtin, A., Vergne, J., Rivera, L., and Dubernet, P. Location of river-induced seismic signal from noise correlation functions. *Geophysical Journal International*, 182(3):1161–1173, 2010. doi: 10.1111/j.1365-246X.2010.04701.x.

Burtin, A., Cattin, R., Bollinger, L., Vergne, J., Steer, P., Robert, A., Findling, N., and Tiberi, C. Towards the Hydrologic and Bed Load Monitoring from High-Frequency Seismic Noise in a Braided River: The "Torrent de St Pierre", French Alps. *Journal of Hydrology*, 408(1-2):43–53, Sept. 2011. doi: 10.1016/j.jhydrol.2011.07.014.

Chmiel, M., Roux, P., and Bardainne, T. High-Sensitivity Microseismic Monitoring: Automatic Detection and Localization of Subsurface Noise Sources Using Matched-Field Processing and Dense Patch Arrays. *GEOPHYSICS*, 84(6):KS211–KS223, Nov. 2019. doi: 10.1190/geo2018-0537.1.

Chmiel, M., Godano, M., Piantini, M., Brigode, P., Gimbert, F., Bakker, M., Courboulex, F., Ampuero, J.-P., Rivet, D., Sladen, A., Ambrois, D., and Chapuis, M. Brief Communication: Seismological Analysis of Flood Dynamics and Hydrologically Triggered Earthquake Swarms Associated with Storm Alex. *Natural Hazards and Earth System Sciences*, 22(5):1541–1558, May 2022. doi: 10.5194/nhess-22-1541-2022.

Cook, K. L., Andermann, C., Gimbert, F., Adhikari, B. R., and Hovius, N. Glacial Lake Outburst Floods as Drivers of Fluvial Erosion in the Himalaya. *Science*, 362(6410):53–57, Oct. 2018. doi: 10.1126/science.aat4981.

Coviello, V., Arattano, M., and Turconi, L. Detecting Torrential Processes from a Distance with a Seismic Monitoring Network. *Natural Hazards*, 78(3):2055–2080, Sept. 2015. doi: 10.1007/s11069-015-1819-2.

Cros, E., Roux, P., Vandemeulebrouck, J., and Kedar, S. Locating Hydrothermal Acoustic Sources at Old Faithful Geyser Using Matched Field Processing: Old Faithful Viewed through Array Processing. *Geophysical Journal International*, 187(1):385–393, Oct. 2011. doi: 10.1111/j.1365-246X.2011.05147.x.

Farin, M., Tsai, V. C., Lamb, M. P., and Allstadt, K. E. A Physical Model of the High-frequency Seismic Signal Generated by Debris Flows. *Earth Surface Processes and Landforms*, 44(13): 2529–2543, Oct. 2019. doi: 10.1002/esp.4677.

Ferguson, R. and Ashworth, P. Spatial patterns of bedload transport and channel change in braided and near braided rivers. *Dynamics of gravel-bed rivers*, page 477, 1992.

Gimbert, F., Tsai, V. C., and Lamb, M. P. A Physical Model for Seismic Noise Generation by Turbulent Flow in Rivers. *Journal of Geophysical Research: Earth Surface*, 119(10):2209–2238, Oct. 2014. doi: 10.1002/2014JF003201.

Gimbert, F., Fuller, B. M., Lamb, M. P., Tsai, V. C., and Johnson, J. P. L. Particle Transport Mechanics and Induced Seismic Noise in Steep Flume Experiments with Accelerometer-embedded Tracers. *Earth Surface Processes and Landforms*, 44(1):219–241, Jan. 2019. doi: 10.1002/esp.4495.

Gimbert, F., Nanni, U., Roux, P., Helmstetter, A., Garambois, S., Lecointre, A., Walpersdorf, A., Jourdain, B., Langlais, M., Laarman, O., Lindner, F., Sergeant, A., Vincent, C., and Walter, F. A Multi-Physics Experiment with a Temporary Dense Seismic Array on the Argentière Glacier, French Alps: The RESOLVE Project. *Seismological Research Letters*, 92(2A):1185–1201, Mar. 2021. doi: 10.1785/0220200280.

Gonzalez, A., Fontaine, F. R., Barruol, G., Recking, A., Burtin, A., Join, J.-L., Delcher, E., Michon, L., and Gimbert, F. Seismic signature of a river flooding in La Reunion Island during the tropical cyclone Dumazile (March 2018). *Journal of Applied Geophysics*, 215:105127, 2023. doi: 10.1016/j.jappgeo.2023.105127.

Johannot, A., Gimbert, F., Fontaine, F., and Recking, A. Bedload regime transition detected with seismic measurements during flood events in a morphodynamically active Alpine river. *Earth Surface Processes and Landforms*, 50, 12 2025. doi: 10.1002/esp.70208.

Kuperman, W. and Turek, G. Matched field acoustics. *Mechanical systems and signal processing*, 11(1):141–148, 1997. doi: 10.1006/mssp.1996.0066.

Lajeunesse, E., Malverti, L., and Charru, F. Bed load transport in turbulent flow at the grain scale: Experiments and modeling. *Journal of Geophysical Research: Earth Surface*, 115(F4), 2010. doi: 10.1029/2009JF001628.

Misset, C., Recking, A., Legout, C., Bakker, M., Bodereau, N., Borgniet, L., Cassel, M., Geay, T., Gimbert, F., Navratil, O., et al. Combining multi-physical measurements to quantify bedload transport and morphodynamics interactions in an Alpine braiding river reach. *Geomorphology*, 351:106877, 2020a. doi: 10.1016/j.geomorph.2019.106877.

Misset, C., Recking, A., Legout, C., Bakker, M., Gimbert, F., Geay, T., and Zanker, S. Data supporting "Using continuous turbidity and seismic measurements to unravel sediment provenance and interaction between suspended and bedload transport in an Alpine catchment". Mendeley Data, Version 1, 2020b. doi: 10.17632/nxvhnjmg8j.1.

Misset, C., Recking, A., Legout, C., Bakker, M., Gimbert, F., Geay, T., and Zanker, S. Using Continuous Turbidity and Seismic Measurements to Unravel Sediment Provenance and Interaction Between Suspended and Bedload Transport in an Alpine Catchment. *Geophysical Research Letters*, 48(4):e2020GL090696, 2021. doi: 10.1029/2020GL090696.

Nanni, U., Gimbert, F., Roux, P., and Lecointre, A. Observing the Subglacial Hydrology Network and Its Dynamics with a Dense Seismic Array. *Proceedings of the National Academy of Sciences*, 118(28):e2023757118, July 2021. doi: 10.1073/pnas.2023757118.

Nanni, U., Roux, P., Gimbert, F., and Lecointre, A. Dynamic Imaging of Glacier Structures at High-Resolution Using Source Localization With a Dense Seismic Array. *Geophysical Research Letters*, 49(6):e2021GL095996, Mar. 2022. doi: 10.1029/2021GL095996.

Nanni, U., Roux, P., and Gimbert, F. Mapping Glacier Structure in Inaccessible Areas From Turning Seismic Sources Into a Dense Seismic Array. *Geophysical Research Letters*, 51(11): e2023GL108058, June 2024. doi: 10.1029/2023GL108058.

Nasr, M., Johannot, A., Geay, T., Zanker, S., Le Guern, J., and Recking, A. Passive Acoustic Monitoring of Bed Load with Drifted Hydrophone. *Journal of Hydraulic Engineering*, 149(7):06023003, 2023. doi: 10.1061/JHEND8.HYENG-13438.

Nasr, M., Johannot, A., Geay, T., Zanker, S., Le Guern, J., and Recking, A. Optimization of passive acoustic bedload monitoring in rivers by signal inversion. *Earth Surface Dynamics*, 12(1): 117–134, 2024. doi: 10.5194/esurf-12-117-2024.

Piantini, M., Gimbert, F., Bellot, H., and Recking, A. Triggering and

Propagation of Exogenous Sediment Pulses in Mountain Channels: Insights from Flume Experiments with Seismic Monitoring. *Earth Surface Dynamics*, 9(6):1423–1439, Nov. 2021. doi: 10.5194/esurf-9-1423-2021.

Piantini, M., Gimbert, F., Bakker, M., Recking, A., and Nanni, U. Using a Dense Seismic Array to Study Fluvial Processes in a Braided River Reach under Flood Conditions. *LHB*, 108(1):2053314, Dec. 2022. doi: 10.1080/27678490.2022.2053314.

Recking, A., Johannot, A., Horita, K., Nasr, M., Vázquez-Tarrío, D., Zanker, S., Fontaine, F., and Melun, G. An attempt to take into account natural variability in 1D bedload prediction. *Journal of Geophysical Research: Earth Surface*, 129(7):e2023JF007601, 2024. doi: 10.1029/2023JF007601.

Revankar, S. V., Gimbert, F., and Recking, A. Data supporting "Frequency-Resolved Seismic Source Localization in Fluvial Settings Using Dense Arrays". Zenodo, 2026. doi: 10.5281/zenodo.18887672.

Ricker, N. The form and laws of propagation of seismic wavelets. *Geophysics*, 18(1):10–40, 1953. doi: 10.1190/1.1437843.

Rindraharisaona, E., Réchou, A., Fontaine, F., Barruol, G., Stamenoff, P., Boudevillain, B., Rigaud-Louise, F., and Delcher, E. Seismic signature of rain and wind inferred from seismic data. *Earth and Space Science*, 9(10):e2022EA002328, 2022. doi: 10.1029/2022EA002328.

Ringler, A. T., Anthony, R. E., Karplus, M., Holland, A., and Wilson, D. C. Laboratory tests of three Z-land fairfield nodal 5-Hz, three-component sensors. *Seismological Research Letters*, 89 (5):1601–1608, 2018. doi: 10.1785/0220170236.

Rodrigues, S., Mosselman, E., Claude, N., Wintenberger, C. L., and Juge, P. Alternate bars in a sandy gravel bed river: generation, migration and interactions with superimposed dunes. *Earth Surface Processes and Landforms*, 40(5):610–628, 2015. doi: 10.1002/esp.3657.

Rost, S. and Thomas, C. Array Seismology: Methods and Applications. *Reviews of Geophysics*, 40(3), Sept. 2002. doi: 10.1029/2000RG000100.

Schmandt, B., Aster, R. C., Scherler, D., Tsai, V. C., and Karlstrom, K. Multiple Fluvial Processes Detected by Riverside Seismic and Infrasound Monitoring of a Controlled Flood in the Grand Canyon. *Geophysical Research Letters*, 40(18):4858–4863, Sept. 2013. doi: 10.1002/grl.50953.

Schmandt, B., Gaeuman, D., Stewart, R., Hansen, S., Tsai, V., and Smith, J. Seismic Array Constraints on Reach-Scale Bedload Transport. *Geology*, 45(4):299–302, Apr. 2017. doi: 10.1130/G38639.1.

Schweitzer, J., Fyen, J., Mykkeltveit, S., Gibbons, S. J., Pirli, M., Kühn, D., and Kværna, T. Seismic arrays. In *New manual of seismological observatory practice 2 (NMSOP-2)*, pages 1–80. Deutsches GeoForschungsZentrum GFZ, 2012. doi: 10.2312/GFZ.NMSOP-2$_c h9$.

Stehly, L., Campillo, M., and Shapiro, N. A study of the seismic noise from its long-range correlation properties. *Journal of Geophysical Research: Solid Earth*, 111(B10), 2006. doi: 10.1029/2005JB004237.

Tao, Y., Tian, B., Adhikari, B. R., Zuo, Q., Luo, X., and Di, B. A Review of Cutting-Edge Sensor Technologies for Improved Flood Monitoring and Damage Assessment. *Sensors*, 24(21):7090, 2024. doi: 10.3390/s24217090.

Thode, A. M., D'Spain, G., and Kuperman, W. Matched-field processing, geoacoustic inversion, and source signature recovery of blue whale vocalizations. *The Journal of the Acoustical Society of America*, 107(3):1286–1300, 2000. doi: 10.1121/1.428417.

Tolstoy, A. Linearization of the matched field processing approach to acoustic tomography. *The Journal of the Acoustical Society of America*, 91(2):781–787, 1992. doi: 10.1121/1.402538.

Tsai, V. C., Minchew, B., Lamb, M. P., and Ampuero, J.-P. A Physical Model for Seismic Noise Generation from Sediment Transport in Rivers. *Geophysical Research Letters*, 39(2):2011GL050255, Jan. 2012. doi: 10.1029/2011GL050255.

Vidale, J. E. Complex polarization analysis of particle motion. *Bulletin of the Seismological society of America*, 76(5):1393–1405, 1986. doi: 10.1785/BSSA0760051393.

Wang, Y. The Ricker wavelet and the Lambert W function. *Geophysical Journal International*, 200(1):111–115, 2015. doi: 10.1093/gji/ggu384.

Wathelet, M., Jongmans, D., Ohrnberger, M., and Bonnefoy-Claudet, S. Array Performances for Ambient Vibrations on a Shallow Structure and Consequences over V s Inversion. *Journal of Seismology*, 12(1):1–19, Jan. 2008. doi: 10.1007/s10950-007-9067-x.

The article *Frequency-Resolved Seismic Source Localization in Fluvial Settings Using Dense Arrays* © 2026 by Samidha V. Revankar is licensed under CC BY 4.0.